Extended imaging conditions for wave-equation migration

Paul Sava[1] & Ivan Vasconcelos[2]
[1]*Center for Wave Phenomena, Colorado School of Mines*
[2]*ION Geophysical and School of Geosciences, University of Edinburgh*

ABSTRACT
Wavefield-based migration velocity analysis using the semblance principle requires computation of images in an extended space in which we can evaluate the imaging consistency as a function of overlapping experiments. Usual industry practice is to assemble those seismic images in common-image-gathers (CIG) which represent reflectivity as a function depth and extensions, e.g. reflection angles. We introduce extended common-image-point (CIP) gathers constructed only as a function of the space- and time-lag extensions at sparse and irregularly distributed points in the image. Semblance analysis using CIPs constructed by this procedure is advantageous because we do not need to compute gathers at regular surface locations and we do not need to compute extensions at all depth levels. The CIPs also give us the flexibility to distribute them in the image at irregular locations aligned with the geologic structure. Furthermore, the CIPs remove the depth bias of CIGs constructed as a function of the depth axis. An interpretation of the CIPs using scattering theory shows that they are scattered wavefields associated with sources and receivers inside the subsurface. Thus, when the surface wavefields are correctly reconstructed, the extended CIPs are characterized by focused energy at the origin of the space- and time-lag axes. Otherwise, the energy defocuses from the origin of the lag axes proportionally with the cumulative velocity error in the overburden. This information can be used for wavefield-based tomographic updates of the velocity model, and if the velocity used for imaging is correct, the coordinate-independent CIPs can be decomposed function of the angles of incidence.

Key words: wave-equation, migration, velocity analysis

1 INTRODUCTION

In regions characterized by complex subsurface structure, wave-equation depth migration is a powerful tool for accurately imaging the earth's interior. The quality of the final image greatly depends on the quality of the velocity model. Thus, constructing accurate velocity is essential for imaging (Gray et al., 2001). In particular, it is important to construct subsurface velocity models using techniques that are consistent with the methods used for imaging.

Generally speaking, there are two possible strategies for velocity estimation from surface seismic data in the context of wavefield depth migration which differ by the implementation domain. One possibility is to formulate an objective function in the *data space*, prior to migration, by evaluating the match between recorded and simulated data using an approximate (background) velocity model. Techniques in this category are known by the name of tomography (or inversion). Another possibility is to formulate an objective function in the *image space*, after migration, by measuring and correcting image features that indicate model inaccuracies. Techniques in this category are known as migration velocity analysis (MVA), since they involve migrated images and not the recorded data directly. In both cases, velocity estimation can be done either using rays or waves as the carrier of information, leading to techniques known by the names of *traveltime tomography* (Bishop et al., 1985; Stork, 1992; Al-Yahya, 1987; Fowler, 1988; Etgen, 1990; Chavent & Jacewitz, 1995; Clement et al., 2001; Chauris et al., 2002a,b; Billette et al., 2003; Lambare et al., 2004; Clapp et al., 2004), or *wave-equation tomography* (Gauthier et al., 1986; Tarantola, 1987; Mora, 1989; Woodward, 1992; Pratt, 1999; Sirgue & Pratt, 2004; Biondi & Sava, 1999; Sava & Biondi, 2004a,b; Shen et al., 2003; Albertin et al., 2006).

The key component for an MVA technique implemented in the image space is the analysis of image attributes which

indicate inaccurate imaging. These attributes are often represented by image extensions, e.g. reflectivity as functions of angle or offset which exploit the **semblance principle** stating that images constructed for different seismic experiments are kinematically similar if the correct velocity is used. This property can be exploited for velocity model building by minimizing objective functions to optimize certain image attributes. For example, we can consider flatness or focusing measured on image gathers, which can be quantified using the generic annihilators as discussed by Symes (2009).

In this paper, we discuss an imaging condition for wavefield-based imaging which can be exploited for velocity model building. This imaging condition is best understood in the context of reverse-time migration since it does not require assumptions about the spatial distribution of reflectors in the subsurface. We construct common-image-point gathers at sparse locations in the image, thus reducing computational cost while preserving velocity model building information. We mainly concentrate on exploring the meaning and features of this imaging condition, on the computational aspects which make implementation of this imaging condition efficient and on measurements that can be made on migrated images to establish the accuracy of the velocity model. How such measurements can be used for migration velocity analysis is a vast subject and we leave it outside the scope of this paper.

2 IMAGING CONDITIONS

Conventional seismic imaging methods share the assumption of single scattering at discontinuities in the subsurface. Under this assumption, waves propagate from seismic sources, interact with discontinuities and return to the surface as reflected seismic waves. We commonly speak about a "source" wavefield, originating at the seismic source and propagating in the medium prior to any interaction with discontinuities, and a "receiver" wavefield, originating at discontinuities and propagating in the medium to the receivers (Berkhout, 1982; Claerbout, 1985). The two wavefields kinematically coincide at discontinuities. Any mismatch between the wavefields indicates inaccurate wavefield reconstruction typically assumed to be due to inaccurate velocity. In this context, we do not need to make geometrical assumptions about up- or down-going propagation, since waves can move in any direction as long as they scatter only once. We also do not need to make any assumption about how we reconstruct those two wavefields as long as the wave-equation used accurately describes wave propagation in the medium under consideration.

We can formulate imaging as a process involving two steps: the wavefield reconstruction and the imaging condition. The key elements in this imaging procedure are the source and receiver wavefields, W_s and W_r. We can represent those wavefields as 4-dimensional objects, either in the time domain (for wavefield reconstruction using the two-way acoustic wave-equation) as a function of space $\mathbf{x} = \{x, y, z\}$ and time t, or in the frequency domain (for wavefield reconstruction using the one-way acoustic wave-equation) as a function of space and frequency ω. For imaging, we need to analyze if the wavefields match kinematically in time and then extract the reflectivity information using an imaging condition operating along the space and time axes.

A conventional cross-correlation imaging condition (cIC) based on the reconstructed wavefields can be formulated in the time or frequency domain as the zero lag of the cross-correlation between the source and receiver wavefields (Claerbout, 1985):

$$R(\mathbf{x}) = \sum_{shots} \sum_{t} W_s(\mathbf{x}, t)\, W_r(\mathbf{x}, t) \tag{1}$$

$$= \sum_{shots} \sum_{\omega} \overline{W_s(\mathbf{x}, \omega)} W_r(\mathbf{x}, \omega)\,, \tag{2}$$

where R represents the migrated image and the over-line represents complex conjugation. This operation exploits the fact that portions of the wavefields match kinematically at subsurface positions where discontinuities occur. Alternative imaging conditions use deconvolution of the source and receiver wavefields, but we do not elaborate further on this subject in this paper since the differences between cross-correlation and deconvolution are not central for our discussion in this paper.

An extended imaging condition preserves in the output image certain acquisition (e.g. source or receiver coordinates) or illumination (e.g. reflection angle) parameters (Clayton & Stolt, 1981; Claerbout, 1985; Stolt & Weglein, 1985; Weglein & Stolt, 1999). In shot-record migration, the source and receiver wavefields are reconstructed on the same computational grid at all locations in space and all times or frequencies, therefore there is no a-priori separation that can be transferred to the output image. In this situation, the separation can be constructed by correlation of the wavefields from symmetric locations relative to the image point, measured either in space (Rickett & Sava, 2002; Sava & Fomel, 2005) or in time (Sava & Fomel, 2006). This separation essentially represents local cross-correlation lags between the source and receiver wavefields. Thus, an extended cross-correlation imaging condition (eIC) defines the image as a function of space and cross-correlation lags in space and time. This imaging condition can also be formulated in the time and frequency domains:

$$R(\mathbf{x}, \boldsymbol{\lambda}, \tau) = \sum_{shots} \sum_{t} W_s(\mathbf{x}-\boldsymbol{\lambda}, t-\tau)\, W_r(\mathbf{x}+\boldsymbol{\lambda}, t+\tau) \tag{3}$$

$$= \sum_{shots} \sum_{\omega} e^{2i\omega\tau} \overline{W_s(\mathbf{x}-\boldsymbol{\lambda}, \omega)} W_r(\mathbf{x}+\boldsymbol{\lambda}, \omega) \tag{4}$$

Equations 1-2 represent a special case of equations 3-4 for $\boldsymbol{\lambda} = 0$ and $\tau = 0$. The eIC defined by equations 3-4 can be used to analyze the accuracy of wavefield reconstruction. Assuming that all errors accumulated in the incorrectly-reconstructed wavefields are due to the velocity model, the extended images could be used for velocity model building by exploiting semblance properties emphasized by the space-lags (Biondi & Sava, 1999; Shen et al., 2003; Sava & Biondi, 2004a,b) and focusing properties emphasized by the time-lag (Faye & Jeannot, 1986; MacKay & Abma, 1992, 1993; Nemeth, 1995, 1996). Furthermore, these extensions can be converted to reflection angles (Weglein & Stolt, 1999; Sava & Fomel, 2003, 2006), thus enabling analysis of amplitude varia-

tion with angle for images constructed in complex areas using wavefield-based imaging.

3 COMPUTATIONAL COST ANALYSIS

The main drawback of the extended imaging conditions 3-4 is that they require a large number of computations corresponding to the size of the image given by the space variable $\mathbf{x}$ and by the number of space and time lags given by variables $\boldsymbol{\lambda}$ and τ. In practice, computing and saving the non-zero cross-correlation lags at all image coordinates for large datasets is infeasible. The complete extended image space has 7 dimensions, although due to cost consideration this space is usually analyzed using subsets. We argue later in this paper that calculation of the full extended image may actually not be necessary. In order to analyze the cost of computing wave-equation images with extensions, we can rewrite the expression of the image obtained by eIC using the notation

$$R\left(x, y, z, \lambda_x, \lambda_y, \lambda_z, \tau\right) \ , \tag{5}$$

where x, y, z represent the space coordinates, $\lambda_x, \lambda_y, \lambda_z$ represent space-lag extensions and τ represents the time-lag extension. Our discussion is limited to the computational cost of the imaging condition and does not refer to the computational cost of wavefield reconstruction. We distinguish the following 4 special cases:

3. 1 1: imaging with no extensions

If we do not use any space and time extensions, the extended image is:

$$R\left(x, y, z, \lambda_x = 0, \lambda_y = 0, \lambda_z = 0, \tau = 0\right) \ . \tag{6}$$

As indicated earlier, this subset of the extended image corresponds to the conventional imaging condition. Figures 1(a)-1(b) show conventional images for the Sigsbee 2A dataset (Paffenholz et al., 2002) for correct and low velocities, respectively. The zero lag images indicate velocity inaccuracy by defocusing of point-like events (diffractors or reflector truncations against faults) and by the existence of crossing events in regions of high reflector curvature. This information can be used for velocity model updates (de Vries & Berkhout, 1984; Harlan et al., 1984; Sava et al., 2005; Fomel et al., 2007).

The computational cost C of cIC is proportional to the product $N_x N_y N_z N_t$, where N_x, N_y, N_z represent the number of samples along the space axes, and N_t represents the number time samples used for imaging using reverse-time migration. A similar argument applies for migration by one-way wavefield extrapolation, in which case we replace the number of time samples N_t with the number of frequencies N_ω used for imaging. In both cases, the product of space grid points and time or frequency grid points coincides to the size of the reconstructed seismic wavefields which control the total cost of migration. We use this cost reference when we analyze other cases.

3. 2 2: imaging with space-lag extensions

A common special case of wave-equation imaging with extensions is represented by images obtained with horizontal space-lag extensions only:

$$R\left(x = x_0, y = y_0, z, \lambda_x, \lambda_y, \lambda_z = 0, \tau = 0\right) \ , \tag{7}$$

where x_0 and y_0 indicate fixed coordinates on the surface. This subset of the extended image corresponds to the so-called space-lag common image gathers (Rickett & Sava, 2002; Sava & Fomel, 2005). Figures 2(a)-2(b) show space-lag gathers for the Sigsbee 2A dataset for correct and low velocities, respectively. The gathers are constructed as a function of depth at fixed surface coordinate $x = 9.25$ km. The space-lag CIGs indicate velocity inaccuracy by defocusing from zero space-lag. In this case, since the Sigsbee 2A data are simulated with off-end acquisition, only the positive side of the defocused events is present in the gather. This information can be used for velocity model updates (Sava & Biondi, 2004a,b; Shen et al., 2003).

Assuming that we are computing the extensions at sparse surface coordinates, we construct CIGs at $N = (\alpha_x N_x)\,(\alpha_y N_y)$ points, where α_x and α_y represent decimation coefficients along coordinates x and y. The computational cost of this type of imaging condition relative to the cost of the cIC is

$$\frac{C_\lambda}{C} \sim \left(\alpha_x N_{\lambda_x}\right)\left(\alpha_y N_{\lambda_y}\right) \ . \tag{8}$$

If $N_{\lambda_i} = 40$ and $\alpha_i = 10^{-1}$ $(i = \{x, y\})$, then $\frac{C_\lambda}{C} \sim 16$.

3. 3 3: imaging with time-lag extension

Another common special case of wave-equation imaging with extensions is represented by images obtained with time-lag extensions only:

$$R\left(x = x_0, y = y_0, z, \lambda_x = 0, \lambda_y = 0, \lambda_z = 0, \tau\right) \ , \tag{9}$$

where x_0 and y_0 indicate fixed coordinates on the surface. This subset of the extended image corresponds to the so-called time-lag common image gathers (Sava & Fomel, 2006). Figures 3(a)-3(b) show time-lag gathers for the Sigsbee 2A dataset for correct and low velocities, respectively. The gathers are constructed as a function of depth at fixed surface coordinate $x = 9.25$ km. The time-lag CIGs indicate velocity inaccuracy by departure of the maximum focusing from zero time-lag. This information can be used for velocity model updates, for example by the techniques of (Brown et al., 2008; Yang & Sava, 2009b).

Assuming that we are computing the extensions at sparse space coordinates as in the preceding case, then the computational cost of this type of imaging condition relative to the cost of cIC is

$$\frac{C_\tau}{C} \sim \alpha_x \alpha_y N_\tau \ . \tag{10}$$

If $N_\tau = 10^2$ and $\alpha_i = 10^{-1}$ $(i = \{x, y\})$, then $\frac{C_\tau}{C} \sim 1$, i.e. a

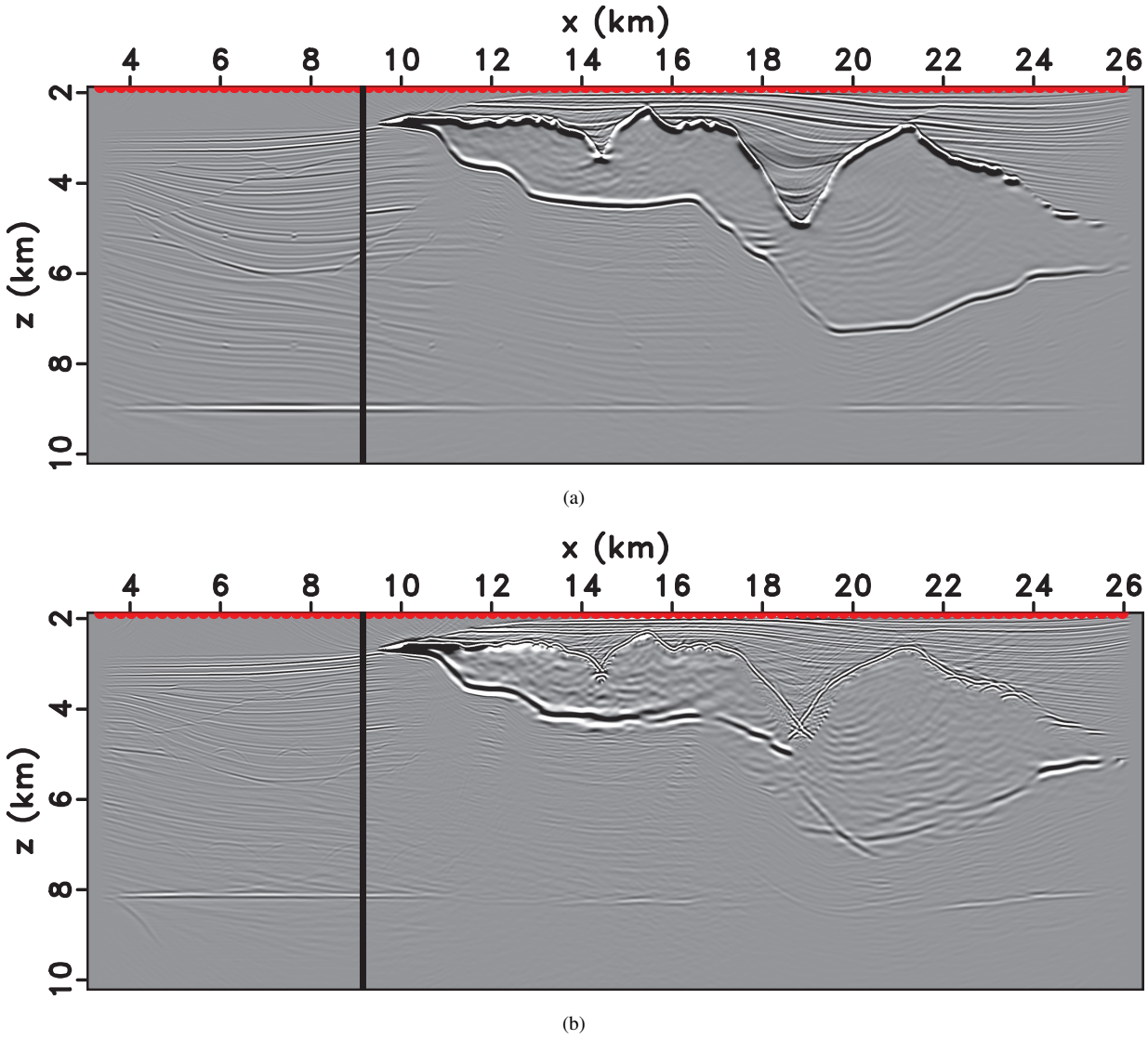


Figure 1. Sigsbee 2A image constructed using (a) correct and (b) low velocities. For the low velocity model, the sediment velocity is 90% of the original.

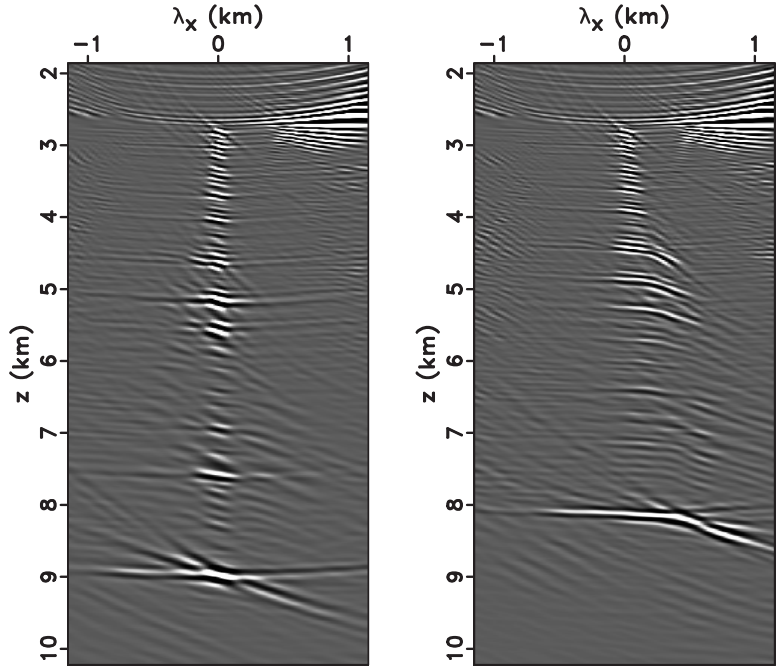


Figure 2. Sigsbee 2A space-lag common-image-gather constructed at $x = 9.25$ km using (a) correct and (b) low velocities. The depth and horizontal space-lag axes are represented to scale.

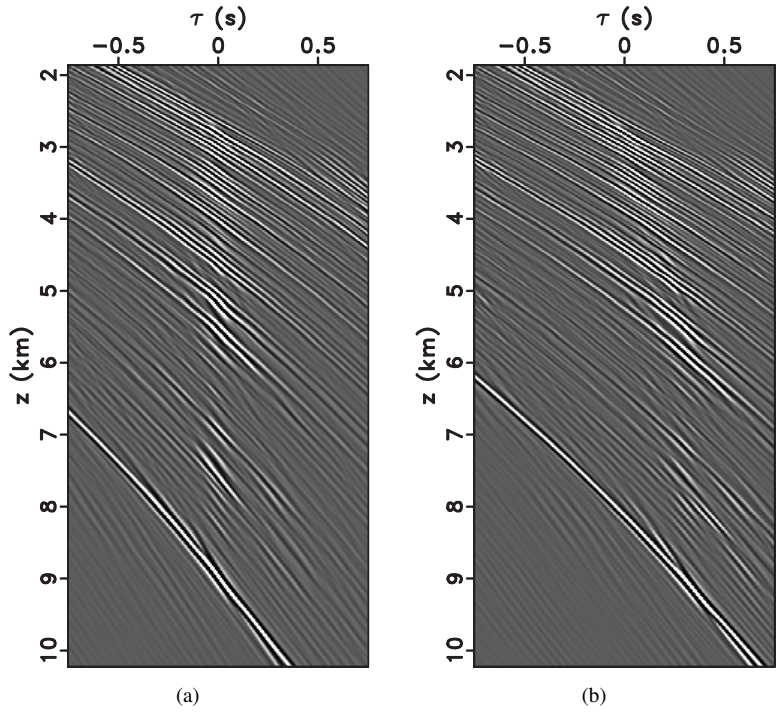


Figure 3. Sigsbee 2A time-lag common-image-gather constructed at $x = 9.25$ km using (a) correct and (b) low velocities.

significantly lower computational cost than the one of imaging with space-lag extensions.

For completeness, we note that a hybrid type of common-image-gather as a function of both space-lags and time-lags can also be computed. Such gathers exploit at the same time the semblance and focusing properties provided by the space-lags and time-lags, respectively (Yang & Sava, 2009a). We can represent such gathers using multidimensional cubes at every location where they are constructed. In this paper, we represent such cube using slices taken at fixed coordinates inside the cube, as indicated in Figures 4(a)-4(b). Figures 5(a)-5(b) show space-lag/time-lag gathers for the Sigsbee 2A dataset for correct and low velocities, respectively. The gathers are constructed as a function of depth at fixed surface coordinate $x = 9.25$ km. The mixed space-lag/time-lag CIGs indicate velocity inaccuracy by defocusing as a function of space-lags and departure of the maximum focusing from zero time-lag. The space-lag and time-lag CIGs discussed earlier represent special cases of this type of gather at $\tau = 0$ or $\boldsymbol{\lambda} = 0$, respectively. The discussion of the relative advantages of using mixed space-lag/time-lag CIGs over the more conventional space-lag or time-lag CIGs falls outside the scope of this paper.

3. 4 4: imaging with space- and time-lag extensions

Another special case of imaging with extensions, which is the main focus of our paper, is at the exact opposite end of the spectrum relative to cIC. Instead of computing images as a function of space coordinates, we can compute images as a function of extensions at fixed locations in the image (only one, in the extreme):

$$R\left(x = x_0, y = y_0, z = z_0, \lambda_x, \lambda_y, \lambda_z, \tau\right) \ , \qquad (11)$$

where x_0, y_0, z_0 indicate fixed coordinates in the image space. Such gathers really correspond to unique image points, thus for the rest of this paper, we use the terminology **common-image-point** (CIP) gathers to emphasize the fact that they refer to single image points.

We assume that we compute extensions at a finite number N of locations in the image. In this case, the total computational cost of this type of imaging condition is

$$\frac{C_{\lambda\tau}}{C} \sim N \frac{N_{\lambda_x} N_{\lambda_y} N_{\lambda_z} N_\tau}{N_x N_y N_z} \ . \qquad (12)$$

As discussed later in the paper, assuming that we can exploit the dip information measured on the image constructed with the conventional imaging condition, we can drop one of the space-lag axes from the computation. For example, if we do not use the vertical space-lag axis (a choice appropriate for nearly-horizontal reflectors), then the computational cost drops one order of magnitude

$$\frac{C_{\lambda\tau}}{C} \sim N \frac{N_{\lambda_x} N_{\lambda_y} N_\tau}{N_x N_y N_z} \ . \qquad (13)$$

We can, in principle, make other choices of space-lag parameters to account for different reflector dips in the image. If $N_i = 10^3$, $N_{\lambda_i} = 40$ ($i = \{x, y\}$), $N_\tau = 10^2$, and $N = 10^3$, then $\frac{C_{\lambda\tau}}{C} \sim 0.2$, i.e. a cost smaller than the one of space-lag imaging, and comparable to the cost of time-lag imaging. We achieve smaller computational cost mainly because we can compute the image as a function of space-lag and time-lag extensions at a relatively small number of points distributed (non-uniformly) in the image, for example along the main reflectors identified in the image by a prior imaging with a cheaper imaging condition, e.g. cIC. This smaller computational cost is attractive for imaging if and only if the space- and time-lag extensions characterize properly the migrated images and, in particular, if they provide information about the velocity model accuracy. We discuss this topic in detail in the following sections.

Finally, we note that the strategy of selecting CIP locations could be used for selecting locations at which to construct CIG's. However, as noted earlier, if using CIGs we would then still be suffering from a bias towards horizontal reflectors in the velocity analysis process.

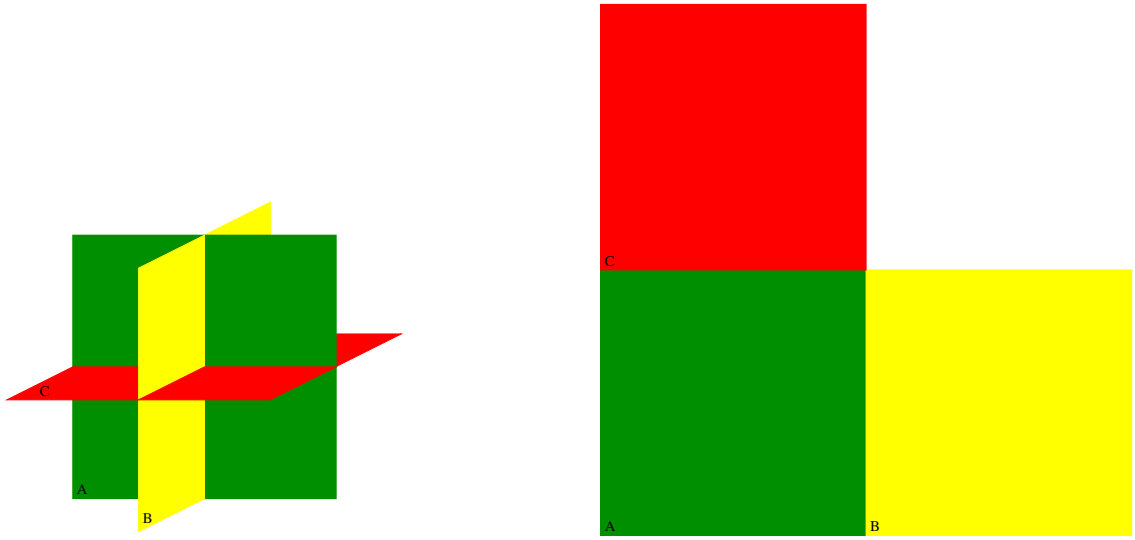
4 COMMON-IMAGE-POINT GATHERS

As indicated earlier, conventional migration velocity analysis is based on the general principle of semblance between images of the interior of the Earth constructed from different seismic experiments. Typically, those experiments represent shots as acquired in the field, but a similar argument applies to other types of experiments synthesized from field data, e.g. plane encoding (Whitmore, 1995) or random encoding (Romero et al., 2000). The collections of images constructed from different experiments are usually organized as a function of surface coordinates at discrete locations. These gathers are refered to as common-image gathers (CIGs), with the understanding that the word "common" refers to the surface position. There are several drawbacks to this type of analysis.

First, due to the typically large computational cost associated with the CIG construction, such gathers are not constructed at all surface positions, but only at a sparse set of coordinates. It is not uncommon that CIGs are constructed, for example, at every 500 m or so in in-line and cross-line directions, which may be **too sparse** for correct evaluation of the image accuracy.

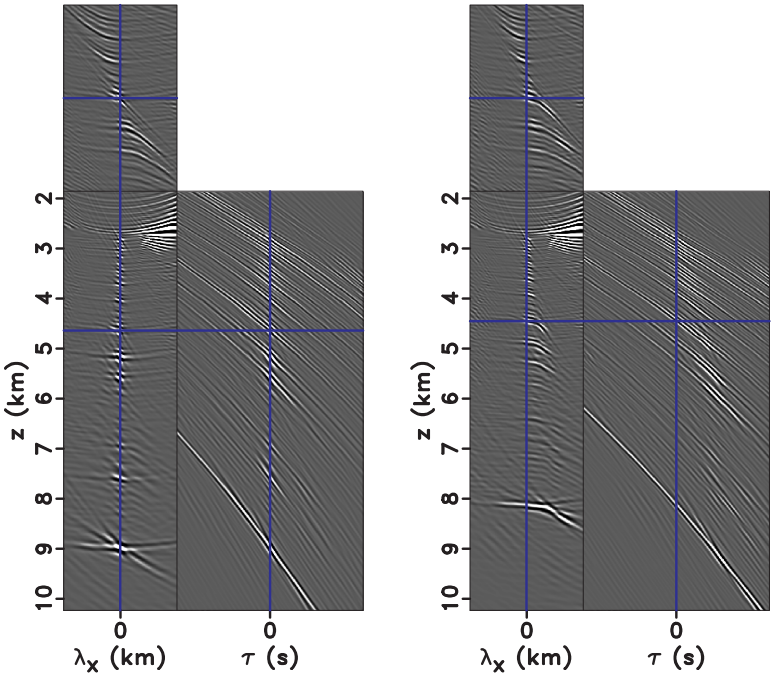
Second, CIGs are usually constructed for fixed surface coordinates, at all depth coordinates. The depth coordinate is finely sampled to describe the seismic wavelet and to capture the rapid variations due to stratigraphic changes. It is not uncommon that the image is sampled every 10 m in depth, which amounts to several (maybe 10 or 20) samples per wavelet. If we are trying to analyze the accuracy of imaging a specific event in the image, this representation may be **too dense** without adding much value for velocity analysis.

Third, the sparse CIG calculation is **independent of the geologic structure**. We see this as a drawback, since it adds no value to compute image extensions at locations that are not useful for velocity analysis, e.g. inside salt bodies. It would make more sense to compute extensions at locations that are



(a) (b)

Figure 4. Orthogonal slices in a 3D cube represented (a) at their true position and (b) at the edges of the cube. The unfolded edge representation allows for unobstructed visualization of the slices. For the cubes used in this paper, panel A represents $z - h_x$ or $h_z - h_x$, panel B represents $z - \tau$ or $h_z - \tau$ and panel C represents $\tau - h_x$.



(a) (b)

Figure 5. Sigsbee 2A space-lag/time-lag common-image-gather constructed at $x = 9.25$ km using (a) correct and (b) low velocities.

driven by the structure itself, rather than at locations chosen by a-priori cost considerations.

Fourth, computing CIGs as a function of the depth axis introduces a **depth bias** which makes those gathers most appropriate for nearly-horizontal structures. For steeply-dipping structures, it makes more sense to compute CIGs as a function of another space axis, e.g. the in-line coordinate (Biondi & Symes, 2004), although even this option preserves an azimuthal ambiguity between the in-line and cross-line directions.

In addressing all those issues, we argue for the construction of common-image-point gathers (CIPs) that are constructed as a function of cross-correlation lags at fixed positions in space. Such CIPs can be computed at image coordinates that are as dense or sparse as the image itself dictates. Furthermore, since no space axis is used in the gather construction, it does not matter whether we analyze nearly-horizontal or nearly-vertical reflectors. All reflectors are equally well resolved, aside from aperture limitations which decrease the velocity discrimination power for steep reflectors when data are acquired on a horizontal datum. The selection of parameters characterizing the extended CIPs, i.e. the $\boldsymbol{\lambda}$ and τ range, depends on the frequency band of the reflection data, as well as on the complexity of the analyzed structure. For lower frequency, we can sample sparsely in the extended domain, but for a wider range of parameters; otherwise, we need to sample more densely but for a lower range of parameters. For simple structures, we can distribute the points where we compute the extensions with low density, while for complex structures we need to distribute such points with higher density. The distribution of CIPs can be irregular and consistent with the geologic structure, thus minimizing the computational cost required to characterize the accuracy for a given image.

We also argue that CIPs constructed at individual points in the image represent a natural choice for reverse-time migration. In this case, waves are extrapolated equally well in all space directions and have no bias toward the depth axis as is the case for conventional downward continuation methods. Likewise, CIPs constructed at fixed image positions do not have a bias toward the depth axis, and can handle waves incident at any angles on reflectors with arbitrary dips and azimuths. The key element used to eliminate the depth bias is the use of the time-lag variable τ.

5 MOVEOUT ANALYSIS

In this section, we discuss the general properties of the common-image-point gathers introduced in the preceding section. We describe the moveout functions for different types of reflectors and for diffractors imaged with correct and incorrect velocities. We formulate analytic moveout functions which give insight into the expected behavior of such CIPs in areas of complex velocity variation.

5. 1 Reflection moveout

Consider the reflection geometry depicted in Figure 6. In the immediate vicinity of the reflection points, we can assume that the source wavefield, the receiver wavefield and the reflector itself can be approximated by planes and we can also assume that the local velocity in this region is constant. The source, receiver and reflector planes are characterized by unit vectors $\mathbf{n}_s$, $\mathbf{n}_r$, and $\mathbf{n}$, respectively. The vectors are linked according to Snell's law by the relations:

$$|\mathbf{n}_s \cdot \mathbf{n}| = |\mathbf{n}_r \cdot \mathbf{n}| = \cos\theta \ , \tag{14}$$

where θ represents the reflection angle measured relative to the reflector normal $\mathbf{n}$.

For a specific reflection event, without loss of generality, we can set the origin of the time axis at the moment when the two planes characterizing the source and receiver wavefields planes intersect at the reflector. Then, we can write the expressions for the source and receiver wavefield planes as

$$\mathbf{n}_s \cdot \mathbf{x} \ = \ 0 \ , \tag{15}$$

$$\mathbf{n}_r \cdot \mathbf{x} \ = \ 0 \ , \tag{16}$$

where $\mathbf{x}$ is a variable spanning the planes.

By construction, the extended imaging condition separates the source and receiver wavefield by shifts in space and time using quantities $\boldsymbol{\lambda}$ and τ, respectively. The expressions for the shifted planes in space and time are

$$\mathbf{n}_s \cdot (\mathbf{x} - \boldsymbol{\lambda}) \ = \ -v\tau \ , \tag{17}$$

$$\mathbf{n}_r \cdot (\mathbf{x} + \boldsymbol{\lambda}) \ = \ +v\tau \ , \tag{18}$$

where v represents the local velocity at the reflection point, assumed to be constant in the region in which the planar assumptions on the source and receiver wavefields holds. Subtracting the expressions 17-18, we obtain

$$(\mathbf{n}_r + \mathbf{n}_s) \cdot \boldsymbol{\lambda} = 2v\tau \ . \tag{19}$$

If we define unit vector $\mathbf{q}$ in the reflection plane, tangent to the reflector (i.e., by construction $\mathbf{q} \cdot \mathbf{n} = 0$), then we can write

$$(\mathbf{q} \cdot \boldsymbol{\lambda}) \sin\theta = v\tau \ . \tag{20}$$

Equation 20 describes the moveout function characterizing a reflection from a single shot-receiver pair in the $\{\boldsymbol{\lambda}, \tau\}$ space, i.e. the space-lags and the time-lag are linearly related by a function which depends on the reflection angle θ, the local velocity v, and by a vector which depends on the reflector dip and reflection azimuth $\mathbf{q}$ (Figure 7(a)). When $\tau = 0$, the moveout function has the form $q_x\lambda_x + q_y\lambda_y + q_z\lambda_z = 0$, i.e. a plane oriented orthogonal to the vector $\mathbf{q}$. When $q_z = 0$, i.e. for a horizontal reflector, the moveout function is $(q_x\lambda_x + q_y\lambda_y)\sin\theta = v\tau$, i.e. the moveout function depends on the local angle of incidence at the reflector and the local reflector slope, Figure 7(a).

We can also express moveout function $s(\boldsymbol{\lambda}, \tau)$ for a single shot-receiver pair using the multidimensional Dirac delta function as (Bracewell, 2006):

$$s(\boldsymbol{\lambda}, \tau) = \delta\left((\mathbf{q} \cdot \boldsymbol{\lambda})\sin\theta - v\tau\right) \ . \tag{21}$$

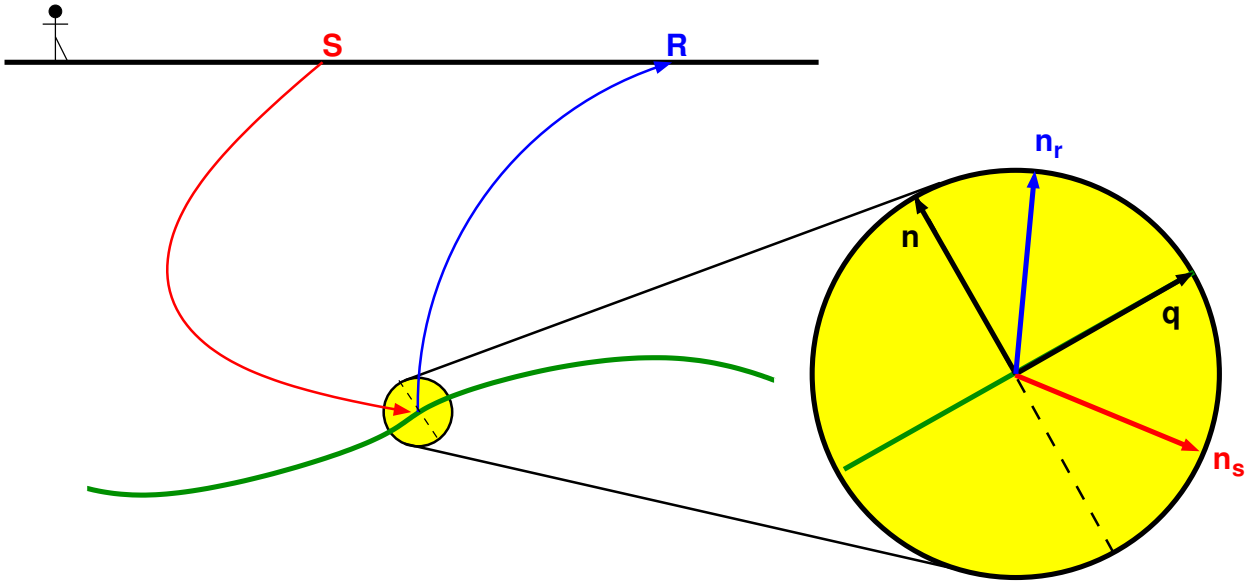


Figure 6. Cartoon illustrating the assumptions made in deriving the moveout functions based on space-lag and time-lag extensions.

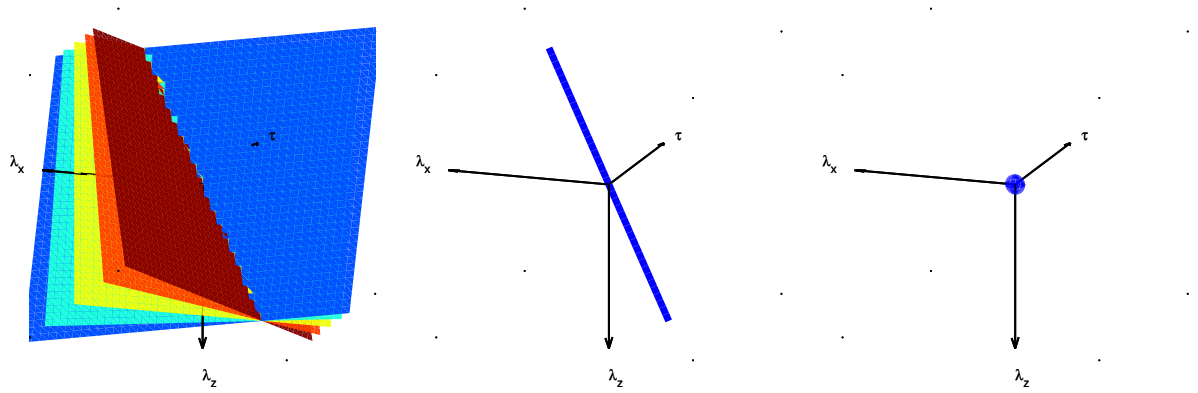


Figure 7. Illustration of (a) the reflection moveout function for individual shots, (b) the reflection moveout function for all shots, and (c) the diffraction moveout function for all shots. Panels (a) and (b) correspond to a reflector dipping at 15°. Panel (a) assumes angles of incidence from -60° to $+60^\circ$.

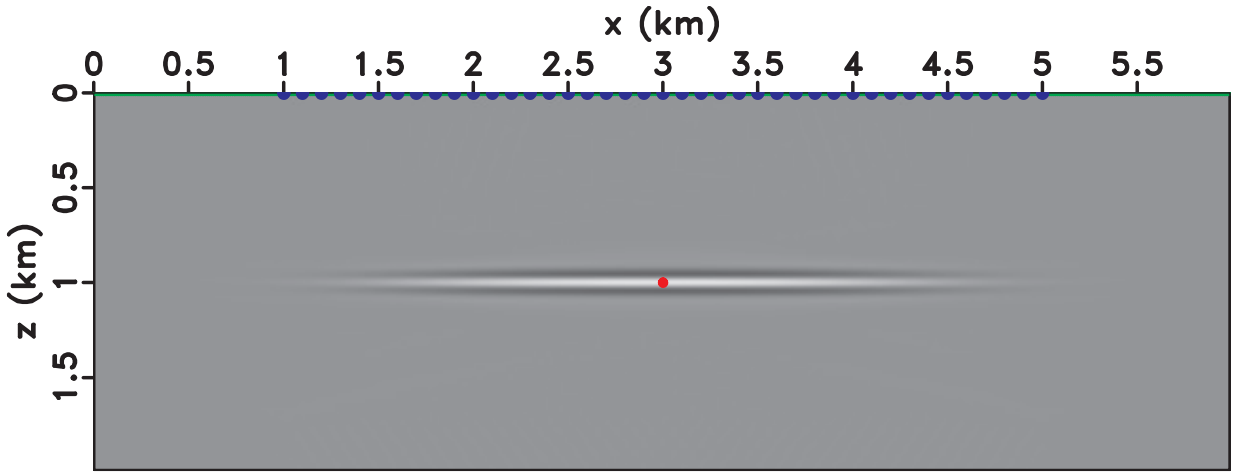
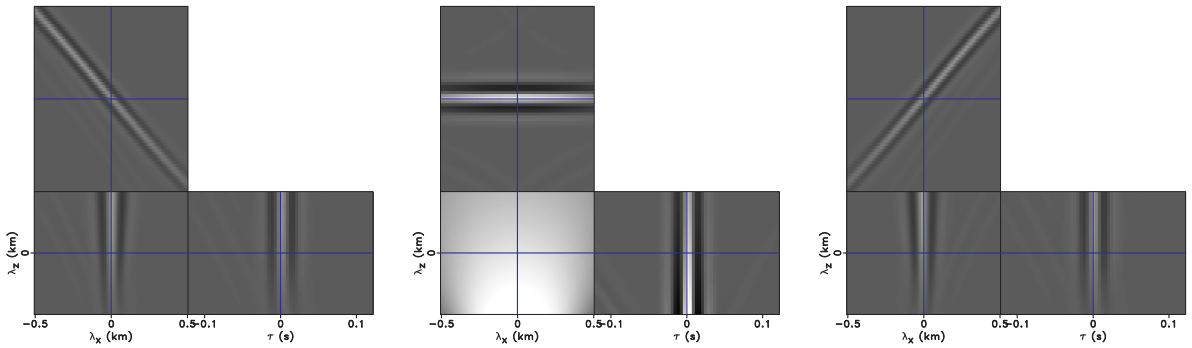


Figure 8. Image of a horizontal reflector in constant velocity media. Sources are distributed along the surface at $z = 0.0$ km between $x = 1.0 - 5.0$ km.



(a) (b) (c)

Figure 9. Common-image-point gathers for a horizontal reflector constructed at $\{x, z\} = \{3.0, 1.0\}$ km from shots located at (a) $\{x = 2.0, z = 0.0\}$ km, (b) $\{x = 3.0, z = 0.0\}$ km, and (c) $\{x = 4.0, z = 0.0\}$ km.

This expression simply indicates that $s(\boldsymbol{\lambda},\tau) = 1$ when $(\mathbf{q}\cdot\boldsymbol{\lambda})\sin\theta = v\tau$ and $s(\boldsymbol{\lambda},\tau) = 0$ otherwise.

For illustration, consider the example shown in Figure 8 corresponding to a horizontal reflector imaged with a constant velocity model. Figures 9(a)-9(c) show CIPs for shots located at coordinates $x = 2.0, 3.0, 4.0$ km, respectively. In all cases, the moveout function for an individual shot is a plane in the $\{\boldsymbol{\lambda},\tau\}$ space depending on the angle of incidence and local velocity. As predicted by the theory, the normal incidence CIP is represented by a plane at $\tau = 0$ and independent of $\boldsymbol{\lambda}$.

In contrast, consider the example shown in Figure 10 corresponding to a dipping reflector imaged with a constant velocity model. Figures 11(a)-11(c) show CIPs for shots located at coordinates $x = 2.0, 3.0, 4.0$ km, respectively. Compared with the CIPs shown in Figures 9(a)-9(c), the moveout depends not only on the angle of incidence and local velocity, but also on the reflector slope.

The moveout characterizing in the $\{\boldsymbol{\lambda},\tau\}$ space a reflection from many shots located on the surface is given by the superposition of events from different sources, i.e. we construct the moveout function $r(\boldsymbol{\lambda},\tau)$ by

$$r(\boldsymbol{\lambda},\tau) = \int d\theta\ \delta\left((\mathbf{q}\cdot\boldsymbol{\lambda})\sin\theta - v\tau\right)\ , \tag{22}$$

therefore

$$r(\boldsymbol{\lambda},\tau) = \delta(\mathbf{q}\cdot\boldsymbol{\lambda})\,\delta(v\tau)\ . \tag{23}$$

Equation 23 indicates that, aside from a scaling factor, the moveout function characterizing a reflector illuminated from many shots is a line at $\tau = 0$ oriented at an angle parallel to the reflector normal (Figure 7(b)). Such events can be seen in Figure 12(b) for the case of the horizontal reflector shown in Figure 8, and in Figure 13(b) for the case of the dipping reflector shown in Figure 10.

5. 2 Diffraction moveout

We can analyze the moveout function characterizing a diffractor in the $\{\boldsymbol{\lambda},\tau\}$ space by noting that we can form point diffractors as a superposition of planar reflectors overlapping at the diffractor position. In this case, we can find the moveout function $d(\boldsymbol{\lambda},\tau)$ by

$$d(\boldsymbol{\lambda},\tau) = \int d\mathbf{q}\ \delta(\mathbf{q}\cdot\boldsymbol{\lambda})\,\delta(v\tau)\ , \tag{24}$$

therefore

$$d(\boldsymbol{\lambda},\tau) = \delta(\boldsymbol{\lambda})\ \delta(v\tau)\ . \tag{25}$$

Equation 25 indicates that, aside from a scaling factor, the moveout function characterizing a diffraction illuminated from many shots is a point at $\tau = 0$ and $\boldsymbol{\lambda} = 0$ (Figure 7(c)). Such an event can be seen in Figure 14(b) for a diffractor located at coordinates $\{x, z\} = \{3.0, 1.0\}$ km, which contrasts with the events evaluated at the same position in the cases of horizontal and dipping reflectors, Figures 12(b) and 13(b), respectively. The apparent vertical stretch is related to the fact that we illuminate this diffractor only from the surface, thus the vertical resolution is poorer than the horizontal resolution.

We note here that the temporal resolution of the extended CIPs is high, both for the case of reflection and for the case of diffractions. This is in contrast with the low temporal resolution of more conventional time-lag gathers (Sava & Fomel, 2006). This observation is important for migration velocity analysis where time picking controls the both resolution and inversion accuracy.

5. 3 Velocity error

An important question to address is what is the impact of imaging with incorrect velocity on the CIPs constructed in the $\{\boldsymbol{\lambda},\tau\}$ domain. We have indicated earlier that the computational cost of constructing such gathers is relatively low since it is simply proportional to the number of points at which lags are evaluated. This is a user-defined parameter and it should reflect the appropriate CIP density necessary to constrain the velocity model. The question is, are those CIPs sensitive to the velocity error?

We address this question with numeric examples. We do not derive moveout functions for incorrect velocity since any such expression would only be valid in simple media, e.g. constant velocity, and not in more complex environments. For velocity analysis we can define a penalty function based on the ideal layout of the CIPs indicated by equations 23 or 25.

Figures 12(a)-14(c) show a comparison of imaging reflectors and diffractors with 3 different velocities, low, correct and high, respectively. In all cases, we track a particular reflection point function of space. This means that the zero lag point of the CIP always characterizes the same seismic event, regardless of its movement due to velocity error. In this experiment, we seek to illustrate that the extended CIPs show velocity inaccuracy even for the case of a complex velocity model imaged with limited-aperture data.

We notice that the shape of the CIPs changes as a function of the velocity model indicating not only that the velocity is erroneous, but also what is the sign of the velocity error. This is true for all types of events, i.e. reflections and diffractions. Since the velocity error is uniform and the velocity model is constant, the moveout function is also uniform indicating similar error from all illumination angles.

The expressions derived in this section are applicable under the assumptions made up-front, i.e. that we operate in the immediate vicinity of the reflection point. In this region, we can approximate the source and receiver wavefields by planes, we can approximate the reflector by a plane and we can assume that the velocity is locally constant. When these assumptions are violated, then the moveout functions discussed here are only accurate for a small range of lag parameters. Otherwise, the discussion made here remains true regardless of the complexity of the velocity model which influences wavefield reconstruction at the considered image point.

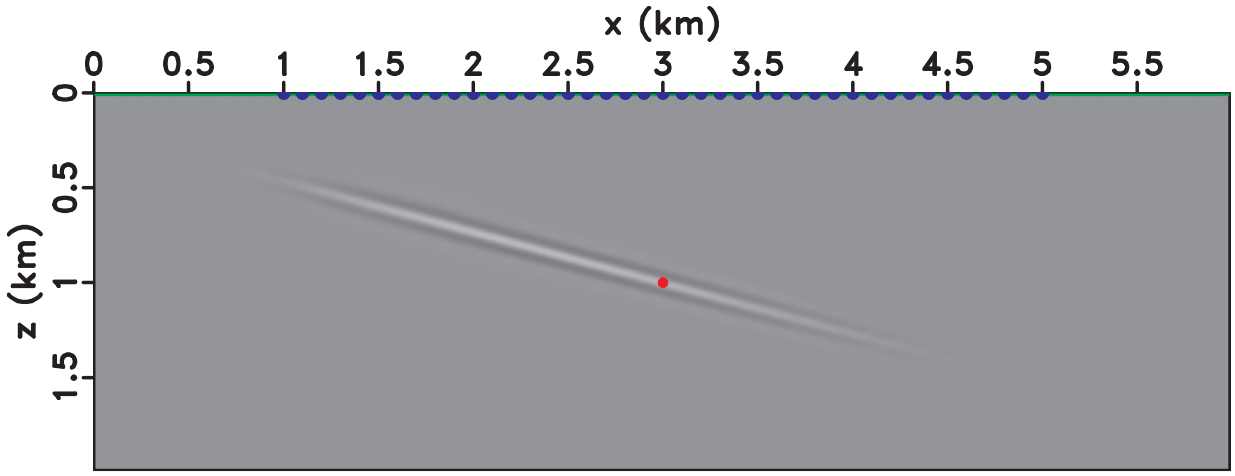
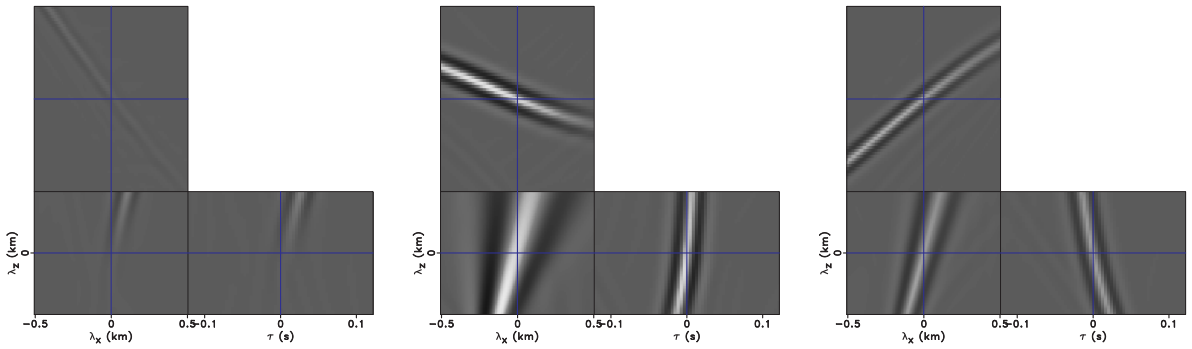
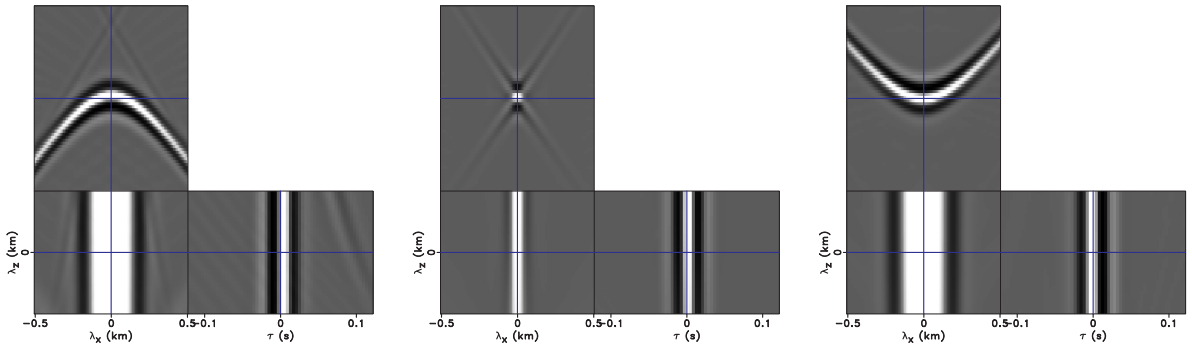


Figure 10. Image of a dipping reflector in constant velocity media. Sources are distributed along the surface at $z = 0.0$ km between $x = 1.0 - 5.0$ km.



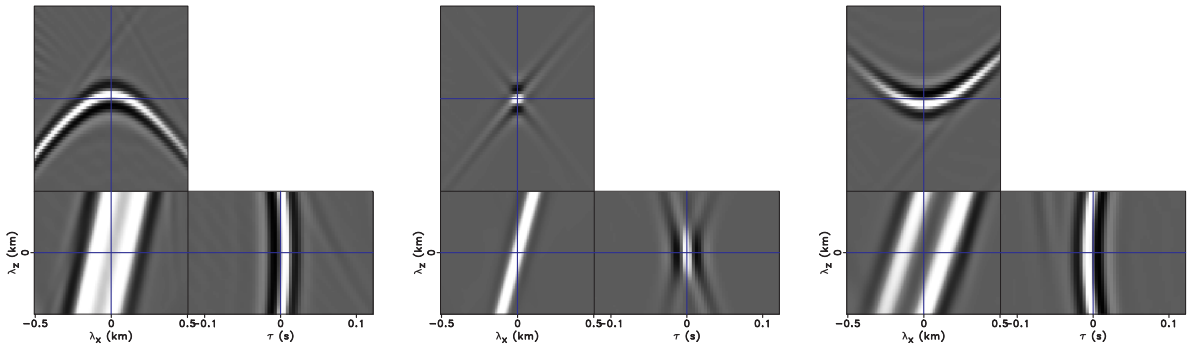
(a) (b) (c)

Figure 11. Common-image-point gathers for a dipping reflector constructed at $\{x, z\} = \{3.0, 1.0\}$ km from shots located at (a) $\{x = 2.0, z = 0.0\}$ km, (b) $\{x = 3.0, z = 0.0\}$ km, and (c) $\{x = 4.0, z = 0.0\}$ km.



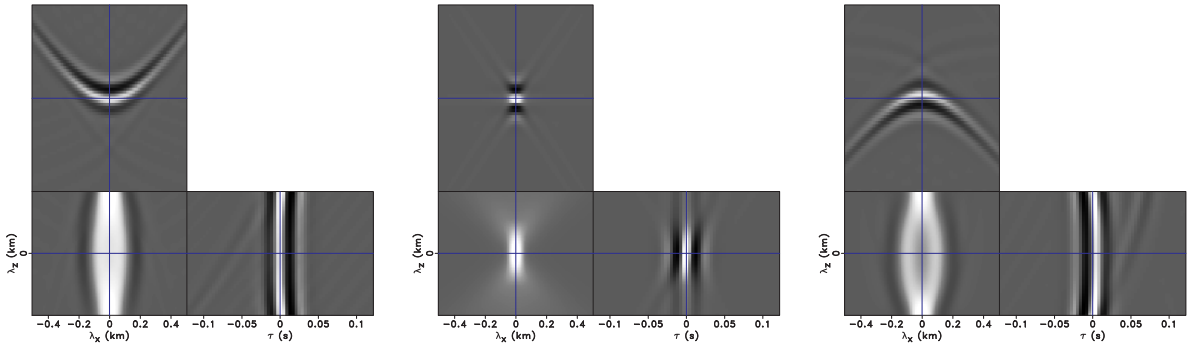
(a) (b) (c)

Figure 12. Common-image-point gathers for a horizontal reflector constructed at $\{x, z\} = \{3.0, 1.0\}$ km from all shots located along the surface at $z = 0.0$ km between $x = 1.0 - 5.0$ km for (a) low velocity, (b) correct velocity, and (c) high velocity.



(a) (b) (c)

Figure 13. Common-image-point gathers for a dipping reflector constructed at $\{x, z\} = \{3.0, 1.0\}$ km from all shots located along the surface at $z = 0.0$ km between $x = 1.0 - 5.0$ km for (a) low velocity, (b) correct velocity, and (c) high velocity.



(a) (b) (c)

Figure 14. Common-image-point gathers for a point diffractor constructed at $\{x, z\} = \{3.0, 1.0\}$ km from all shots located along the surface at $z = 0.0$ km between $x = 1.0 - 5.0$ km for (a) low velocity, (b) correct velocity, and (c) high velocity.

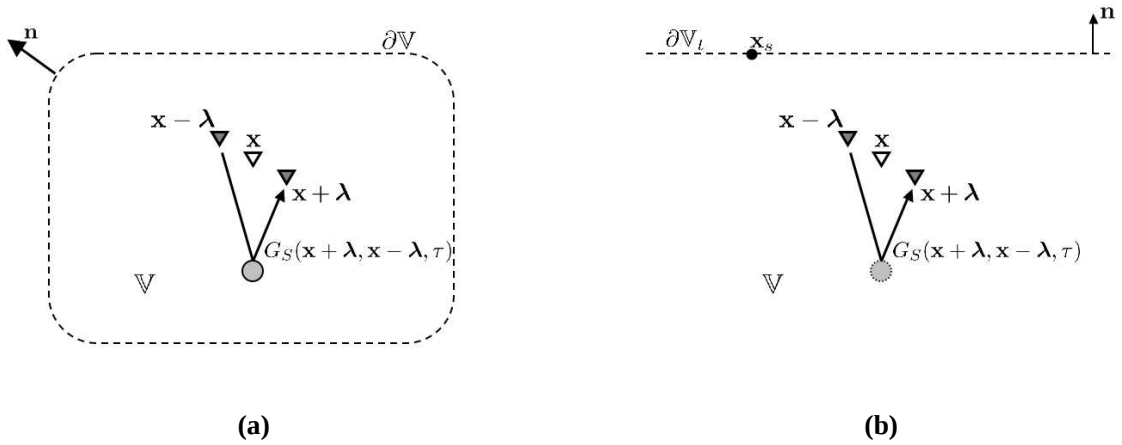


Figure 15. Extended images can be described explicitly in terms of scattered wavefields. As such, an extended image at x correspond to the scattering response $G_S(\mathbf{x}+\boldsymbol{\lambda},\mathbf{x}-\boldsymbol{\lambda},\tau)$ due to a pseudo-source at $\mathbf{x}-\boldsymbol{\lambda}$ recorded by a pseudo-receiver at $\mathbf{x}+\boldsymbol{\lambda}$. These cartoons illustrate the differences in evaluating an extended image at x according (a) equation 28 and (b) to equation 30. The grey circle in both cartoons denotes a finite-size scatterer, where in (a) the scatterer is contoured with a solid line to indicate the presence of model singularities (i.e., sharp boundaries), while in (b) the dotted-line contour represents the use of a smooth background model.

6 DESCRIPTION OF THE EXTENDED IMAGES USING SCATTERING THEORY

The extended imaged described in the earlier sections can be interpreted in a more general sense using scattering theory. An imaging condition for migration by wavefield extrapolation can be physically defined in terms of a scattered field G_S, as

$$R(\mathbf{x}) = G_S(\mathbf{x},\mathbf{x},\tau=0)\ . \tag{26}$$

According to this definition, the conventional image $R(\mathbf{x})$ can be thought of a zero-offset scattered field for source and receiver coinciding at the image point $\mathbf{x}$, evaluated at zero time. Here, we use standard notation for the Green's functions, i.e., $G_S(\mathbf{x},\mathbf{y},\tau)$ corresponds to a scattered-wave response recorded at $\mathbf{x}$ due to a source at $\mathbf{y}$. Since waves in the subsurface travel with finite wave speeds, the zero-offset scattered-wave response in equation 26 is zero when $\mathbf{x}$ is away from scatterers or interfaces, and it is finite when the image point is at a scatterer or interface. This definition is analogous to the "exploding reflector" concept (Loewenthal et al., 1976; Claerbout, 1985). Based on the definition in equation 26, an extended image can be readily defined by evaluating the scattered field G_S for finite source-receiver offsets and at nonzero times, that is

$$R(\mathbf{x},\boldsymbol{\lambda},\tau) = G_S(\mathbf{x}+\boldsymbol{\lambda},\mathbf{x}-\boldsymbol{\lambda},\tau)\ . \tag{27}$$

An exact correlation-type representation of Green's functions characterizing the scattered wavefield for a source located at coordinates $\mathbf{x}-\boldsymbol{\lambda}$, a receiver located at coordinates $\mathbf{x}+\boldsymbol{\lambda}$ and scatterers distributed at coordinates $\mathbf{x}$ in a medium of volume $\mathbb{V}$ surrounded by surface $\partial\mathbb{V}$, Figure 15, is given by the expression (Vasconcelos, 2008; Vasconcelos et al., 2009a):

$$\begin{aligned} G_S(\mathbf{x}+\boldsymbol{\lambda},\mathbf{x}-\boldsymbol{\lambda},\tau) &= \oint_{\mathbf{x}_s\in\partial\mathbb{V}} d^2\mathbf{x}_s \sum_\omega e^{2i\omega\tau}\frac{1}{i\omega\rho}\left[\overline{G_0(\mathbf{x}-\boldsymbol{\lambda},\mathbf{x}_s,\omega)}\nabla G_S(\mathbf{x}+\boldsymbol{\lambda},\mathbf{x}_s,\omega)\right]\cdot\mathbf{n} \\ &- \oint_{\mathbf{x}_s\in\partial\mathbb{V}} d^2\mathbf{x}_s \sum_\omega e^{2i\omega\tau}\frac{1}{i\omega\rho}\left[G_S(\mathbf{x}+\boldsymbol{\lambda},\mathbf{x}_s,\omega)\overline{\nabla G_0(\mathbf{x}-\boldsymbol{\lambda},\mathbf{x}_s,\omega)}\right]\cdot\mathbf{n} \\ &+ \int_{\mathbf{x}_s\in\mathbb{V}} d^3\mathbf{x}_s \sum_\omega e^{2i\omega\tau}\frac{1}{i\omega\rho}G(\mathbf{x}+\boldsymbol{\lambda},\mathbf{x}_s,\omega)\mathcal{V}(\mathbf{x}_s)\overline{G_0(\mathbf{x}-\boldsymbol{\lambda},\mathbf{x}_s,\omega)}\ . \end{aligned} \tag{28}$$

In equation 28, $\mathbf{x}_s$ represents source positions distributed along the surface $\partial\mathbb{V}$, $\mathcal{V}(\mathbf{x}_s)=\omega^2(v^{-2}(\mathbf{x}_s)-v_0^{-2}(\mathbf{x}))$ is the *scattering potential* (v is the migration velocity model, v_0 is a reference velocity model), G_S is the scattered wavefield due to $\mathcal{V}(\mathbf{x}_s)$, G_0 is the reference wavefield, and $G=G_0+G_S$ is the total wavefield. Within the context of migration/inversion, the scattering potential $\mathcal{V}$ is typically said to contain the singular part, i.e., the sharp boundaries, of the desired Earth model while the background wavespeed v_0 is assumed to be smooth (Symes, 2009). While this is simply one conventional for the meaning of $\mathcal{V}$, we note that equation 28 is valid for whichever definition or interpretation is chosen for the scattering potential. For the sake of argument, however, in this manuscript we restrict ourselves to the interpretation that $\mathcal{V}$ represents the sharp contrasts in the Earth model. Equation 28 requires the evaluation

of an integral over the whole subsurface volume $\mathbb{V}$, as well as an integral over its bounding surface $\partial\mathbb{V}$. In this expression, $\mathbf{n}$ denotes the unit normal vector on $\partial\mathbb{V}$. The gradients in the integrands of equation 28 are taken at surface coordinates $\mathbf{x}_s$, and physically represent dipole source (i.e., particle-velocity), in addition to monopole sources (i.e., pressure) along the entire surface $\partial\mathbb{V}$. In order for equation 28 to be written in terms of integrals over source positions $\mathbf{x}_s$, we rely on source-receiver reciprocity (Fokkema & Van Den Berg, 1993) to modify the original version of the correlation-type scattering representations (Vasconcelos et al., 2009a). In migration and imaging, implicit within the integrals on the right-hand side of equation 28 is the concept of "double focussing", since apart from the explicit integration over sources $\mathbf{x}_s$ there is an implicit summation over receivers as the extrapolated fields $G_{0,S}(\mathbf{x} \pm \boldsymbol{\lambda}, \mathbf{x}_s, \omega)$ in the integrands consist of the superposition of extrapolating the signals of all receivers for a given source at $\mathbf{x}_s$ (Halliday et al., 2009).

Computing the scattered wavefield in a medium using the integrals in equation 28 is not practical in exploration seismic experiments for three main reasons. First, the number of sources is limited, and typically available only on the surface of the Earth, i.e. the sources $\mathbf{x}_s$ are available on a subset $\partial\mathbb{V}_t$ of $\partial\mathbb{V}$. Second, receivers are also only available at the Earth's surface or have limited subsurface coverage (e.g., in VSP experiments) and therefore responses for receivers at $\mathbf{x} \in \mathbb{V}$ required by the integrands are not readily available. Third, the quantity $\mathcal{V}(\mathbf{x})$ in the integrand of the volume term assumes perfect knowledge of the velocity model, which is also not available in practice.

For conventional implementation of reverse-time migration, the following assumptions are being made:

$$\begin{cases} i)\text{the singularities in the model are ignored in migration,} & \text{sing supp}(\mathcal{V}(\mathbf{x}_s)) = 0; \\ ii)\text{sources are distributed on a finite surface,} & \mathbf{x}_s \in \partial\mathbb{V}_t; \\ iii)\text{sources are located in the far field;} & \\ iv)\text{the reference field is given by the source wavefield,} & G_0(\mathbf{x}-\boldsymbol{\lambda}, \mathbf{x}_s, \omega) \approx W_s(\mathbf{x}-\boldsymbol{\lambda}, \omega); \\ v)\text{the scattered field is given by the receiver wavefield,} & G_S(\mathbf{x}+\boldsymbol{\lambda}, \mathbf{x}_s, \omega) \approx W_r(\mathbf{x}+\boldsymbol{\lambda}, \omega); . \end{cases} \tag{29}$$

Condition $i)$ states that the true Earth model is unknown, therefore migration uses a smooth migration velocity model, from which we obtain $\mathcal{V}(\mathbf{x}_s)$. Condition $ii)$ states that the integral over closed surface $\partial\mathbb{V}$ is replaced by an integral over an open surface $\partial\mathbb{V}_t$, e.g. sources are located only along the surface. Condition $iii)$ states that because dipole sources are not available in conventional exploration seismic surveys, they are replaces by monopole sources. This assumption is only valid in the far field (Wapenaar & Fokkema, 2006). Finally, conditions $iv)$ and $v)$ state that we approximate the Green's functions G_0 and G_S in the subsurface by wavefields reconstructed from the recorded data based on the smooth background velocity model. These wavefields are evaluated numerically by solving a wave-equation whose coefficients are given by the migration velocity model $v_0(\mathbf{x})$. Therefore, under the assumptions listed in equation 29, wavefield imaging using reverse-time migration approximates the scattered wavefield G_S in equation 28 by evaluating only the surface integral

$$\begin{aligned} \mathcal{I}_{\text{surf}}(\mathbf{x}+\boldsymbol{\lambda}, \mathbf{x}-\boldsymbol{\lambda}, \tau) &\approx \oint_{\mathbf{x}_s \in \partial\mathbb{V}_t} d^2\mathbf{x}_s \sum_{\omega} e^{2i\omega\tau} \frac{2}{c\rho} \left[\overline{G_0(\mathbf{x}-\boldsymbol{\lambda}, \mathbf{x}_s, \omega)} G_S(\mathbf{x}+\boldsymbol{\lambda}, \mathbf{x}_s, \omega) \right] \\ &\approx \oint_{\mathbf{x}_s \in \partial\mathbb{V}_t} d^2\mathbf{x}_s \sum_{\omega} e^{2i\omega\tau} \overline{W_s(\mathbf{x}-\boldsymbol{\lambda}, \omega)} W_r(\mathbf{x}+\boldsymbol{\lambda}, \omega) \ . \end{aligned} \tag{30}$$

The surface integral in Equation 30 represents exactly the extended image in equation 4, if we replace the integral of the open surface $\partial\mathbb{V}_s$ with a simple summation over shots:

$$R(\mathbf{x}, \boldsymbol{\lambda}, \tau) \approx \mathcal{I}_{\text{surf}}(\mathbf{x}+\boldsymbol{\lambda}, \mathbf{x}-\boldsymbol{\lambda}, \tau) \ . \tag{31}$$

We can conclude that Equation 30 is adequate if the imaging objective is to map correctly the reflectors in the subsurface using a smooth background velocity model. The comparison between the two expressions also shows that the images $R(\mathbf{x}, \boldsymbol{\lambda}, \tau)$ simply represent scattered wavefields in the extended space of $\boldsymbol{\lambda}$ and τ. We note that using only the surface term to estimate the extended image implicitly corresponds to the single-scattering assumption. To properly migrate multiply-scattered energy (i.e., multiples) the velocity model must contain singularities (i.e., hard interfaces) for the wavefields W_s and W_r to properly position multiple reflections, therefore using only the surface integral may not be sufficient (Vasconcelos et al., 2009b).

The key insight gained by analyzing the extended images via scattering representations is that extended images are, in fact, estimates of scattered wavefields associated to sources and receivers inside the subsurface. Therefore, we can think of fully extended seismic images as dynamic objects whose behavior is described by wave-equations based on the known velocity model. This idea can be exploited in practice using stationary-phase analysis of equation 30 (Vasconcelos et al., 2009b), as discussed in this paper.

As presented here, our formulation of extended images establishes a formal, explicit connection between the fields of seismic imaging and seismic interferometry. In seismic interferometry the cross-correlation of wavefields received at two receivers allows the extraction of the response between these receivers as if one of them acts as a source (Wapenaar & Fokkema, 2006; Vasconcelos et al., 2009b). While most interferometry applications rely on reciprocity formulations for full wavefields (Wapenaar & Fokkema, 2006), a similar response for only the scattered field traveling from one point inside the medium to another can be found using

scattering reciprocity relations (Vasconcelos et al., 2009b). Since an image of a scatterer can be obtained by collapsing the recorded scattered wavefield onto the scatterer location, this formulation based on scattering representations can be used to interpret the imaging condition in the context of seismic interferometry (Vasconcelos, 2008): the image is the zero-time scattered-wave response generated by zero-offset pseudo-experiments in the image domain. Here we expand on this notion of "image-domain interferometry" and show that the representation theorems for the scattered field allow the extended images to be described as scattered wavefields which are "excited" and "recorded" in the image domain, as illustrated by Figure 15.

Finally, while in this manuscript we only briefly discuss the role of the volume term in equation 28, we must also point out that a more complete understanding on how to deal with this volume integral is subject of ongoing research. We know at the moment that the volume integrals play a crucial role in describing behavior of the extended images that is nonlinear on the unknown Earth model i.e., in describing proper amplitude behavior or in migrating multiples. In fact, we hypothesize that the previously reported "reverse-time migration artifacts" (Fletcher et al., 2006; Guitton et al., 2006) that appear when using rough velocity models (i.e., models with singularities) are likely to be intrinsically related to ignoring the volume terms discussed above.

7 SIGSBEE 2A EXAMPLE

In this section, we illustrate the CIP construction described in the preceding sections with the Sigsbee 2A model. For the CIPs shown here, we consider a fixed reflector in the image and track it at different positions as a function of the velocity model used for imaging. This is legitimate since the only way we can identify a reflector is by observing it in the conventional image at zero lags in space and time. We refer to the images shown in Figures 1(a) and 1(b) to identify CIP locations.

Figures 16(a)-16(c)-16(e) show one CIP for the reflector located at $\{x, z\} = \{9.7, 4.6\}$ km in the image constructed with the correct velocity, Figure 1(a). The various panels correspond to different shots located on the surface at coordinates $x = \{5.16, 6.99, 8.82\}$ km. Similarly, Figures 16(b)-16(d)-16(f) show one CIP for the reflector located at $\{x, z\} = \{9.6, 4.4\}$ km in the image constructed with the low velocity, Figure 1(b). In both situations, we observe that the CIPs for different shots change as a function of the shot position, i.e. they change as a function of the angle of incidence. This observation enables us to speculate that we can use these CIPs to decompose the reflectivity function of the angle of incidence at various positions in the image using slant-stacks similar to the technique used by Sava & Fomel (2003) for more conventional space-lag gathers.

We can also observe that in the case of CIPs constructed with correct velocity, the events corresponding to different shots intersect at zero lag in space and time, indicating correct imaging. In contrast, in the case of CIPs constructed with incorrect velocity, the events corresponding to different shots do not intersect at zero lag in space and time, indicating incorrect imaging. This observation can be further analyzed in the CIPs obtained by stacking of contributions from different shots, as shown in Figure 17(a) for correct velocity and in Figure 17(b) for incorrect velocity. The CIPs constructed with correct velocity are focused around zero in the $\boldsymbol{\lambda} - \tau$ space, while the CIPs constructed with low velocity show events with moveout in the $\boldsymbol{\lambda} - \tau$ space. The complicated, wavefield-like behavior of the extended images as a function of space and time lags can be described by the physics of scattered fields, as discussed in the preceding sections. The fact that the extended CIPs here only show nonzero scattered-wave responses on positive times for positive space lags or negative times for negative space lags is due to the physical aperture limitations of the towed marine acquisition used in the modeling of Sigsbee 2A data.

In general, for arbitrary distribution of velocity anomalies in the overburden, there is no analytic function characterizing those CIPs. For the case we consider here, i.e. uniform scaling of the sediment velocity in the overburden, the events show nearly hyperbolic moveout. The curvature of the events passing through the zero lag point is indicative of velocity error, but it characterizes the cumulative contributions of all velocity anomalies in the overburden relative to this image point. Unraveling this effective contribution requires a tomographic procedure minimizing a global objective function, as indicated earlier in the paper.

Finally, we note that the gather in Figure 17(a) represents a reflector and not a diffractor and that imaging was performed with correct velocity. Furthermore, we can also identify the dip of the reflector without additional measurements in the image space. In contrast, the gather shown in Figure 18(a) corresponds to the superposition between a diffractor and a reflector, as indicated by the apparent focus in the space-lag panel. The focus is not perfect due to the limited aperture of the surface acquisition array. For imaging with incorrect velocity, Figure 18(b), the CIP is not focused.

8 CONCLUSIONS

Extended common-image-point gathers are effective tools for analyzing velocity accuracy for wave-equation imaging. The extended CIPs can be analyzed at sparse locations in the image volume, thus reducing the computational cost of this imaging condition. One possibility is to construct extended CIPs along the main reflectors which are the most indicative velocity model building components of migrated images. The sparse CIP allows for easier visualization and interpretation of extended images. The CIP construction can be further accelerated if we avoid constructing extensions in the direction orthogonal to the reflector dip. Such CIPs are also not biased toward reflectors with specific dips (e.g. nearly-horizontal), thus making them a natural choice for reverse-time migration.

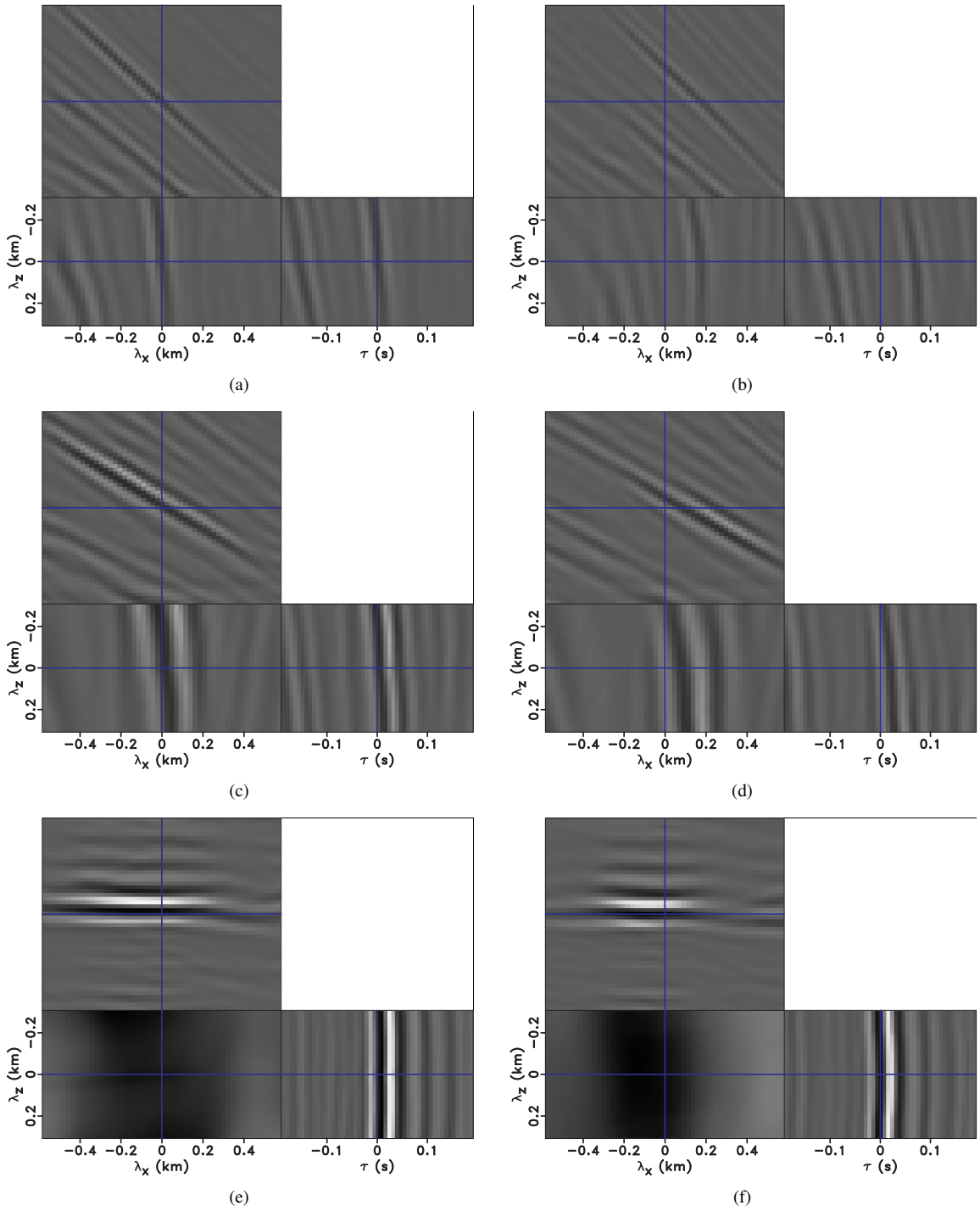
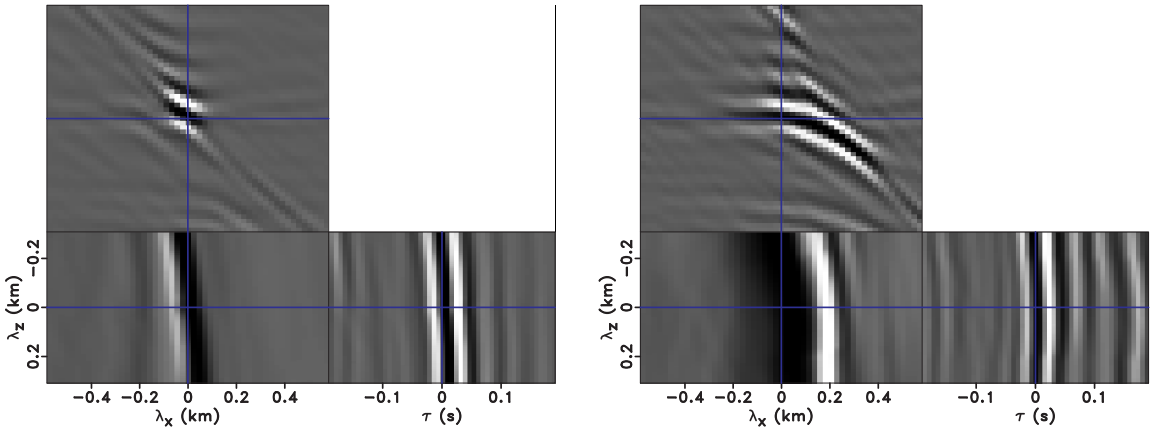
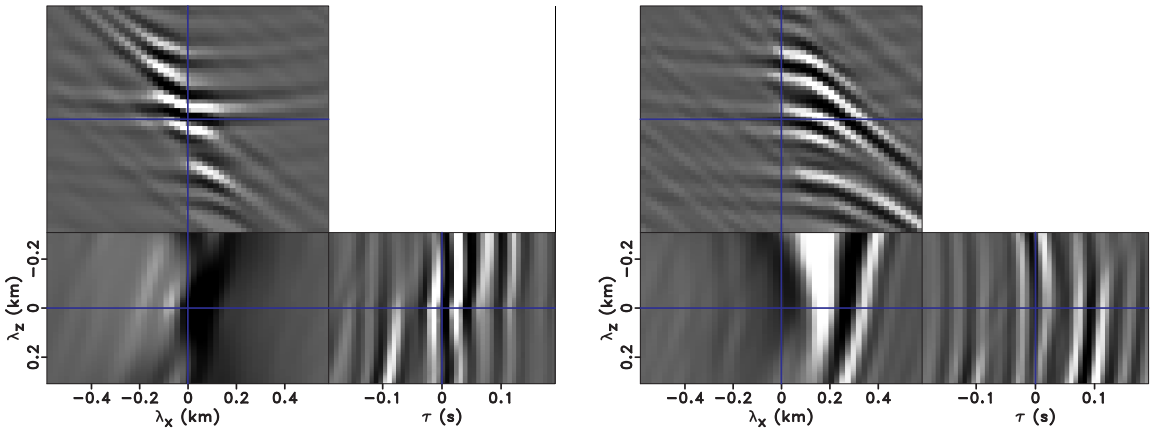


Figure 16. Sigsbee 2A common-image-point gathers constructed for different shots at coordinates $x = \{5.16, 6.99, 8.82\}$ km. Panels (a)-(c)-(e) correspond to coordinates $\{x, z\} = \{9.7, 4.6\}$ km in the image constructed with the correct velocity, Figure 1(a), and panels (b)-(d)-(f) correspond to coordinates $\{x, z\} = \{9.6, 4.4\}$ km in the image constructed with the low velocity, Figure 1(b).



(a) (b)

Figure 17. Sigsbee 2A common-image-point gathers constructed for all shots. Panel (a) corresponds to coordinates $\{x, z\} = \{9.7, 4.6\}$ km in the image constructed with the correct velocity, Figure 1(a), and panel (b) correspond to coordinates $\{x, z\} = \{9.6, 4.4\}$ km in the image constructed with the low velocity, Figure 1(b). The image at this locations corresponds to a slanted reflector.



(a) (b)

Figure 18. Sigsbee 2A common-image-point gathers constructed for all shots. Panel (a) corresponds to coordinates $\{x, z\} = \{7.65, 5.15\}$ km in the image constructed with the correct velocity, Figure 1(a), and panel (b) correspond to coordinates $\{x, z\} = \{7.65, 4.87\}$ km in the image constructed with the low velocity, Figure 1(b). The image at this location corresponds to the superposition between a reflector and a diffractor embedded in the model.

A key requirement for the effectiveness of this technique is that space-lags and time-lag extensions be analyzed simultaneously. This is particularly the case when defining objective functions which penalize CIPs for departure from their ideal geometry. In this situation, we can use scattering theory to interpret the CIPs as scattered wavefields corresponding to sources inside the model. These scattered wavefields have special properties which depend on the the quality of the velocity model used for reconstruction of the source and receiver wavefields from the surface. In addition to velocity analysis, potential applications the CIPs described in this paper include wide-azimuth angle-domain amplitude analysis, as well as slope estimation and separation of reflections and diffractions.

9 ACKNOWLEDGMENTS

Ivan Vasconcelos acknowledges ION Geophysical for support of this research.

REFERENCES

Al-Yahya, K., 1987, Velocity analysis by iterative profile migration: , PhD thesis, Stanford University.

Albertin, U., Sava, P., Etgen, J., and Maharramov, M., 2006, Image differencing and focusing in wave-equation velocity analysis: 68th Mtg., Eur. Assoc. Expl. Geophys., Abstracts.

Berkhout, A. J., 1982, Imaging of acoustic energy by wave field extrapolation: , Elsevier.

Billette, F., Begat, S. L., Podvin, P., and Lambare, G., 2003, Practical aspects and applications of 2D sterotomography: Geophysics, **68**, no. 3, 1008–1021.

Biondi, B., and Sava, P., 1999, Wave-equation migration velocity analysis: 69th Annual International Meeting, SEG, Expanded Abstracts, 1723–1726.

Biondi, B., and Symes, W., 2004, Angle-domain common-image gathers for migration velocity analysis by wavefield-continuation imaging: Geophysics, **69**, no. 5, 1283–1298.

Bishop, T. N., Bube, K. P., Cutler, R. T., Langan, R. T., Love, P. L., Resnick, J. R., Shuey, R. T., Spindler, D. A., and Wyld, H. W., 1985, Tomographic determination of velocity and depth in laterally varying media: Geophysics, **50**, no. 06, 903–923.

Bracewell, R., 2006, Fourier analysis and imaging: , Springer.

Brown, M., Higginbotham, J., and Clapp, R., 2008, Velocity model building with wave equation migration velocity focusing analysis: 77th Annual International Meeting, SEG, Expanded Abstracts, 3083–3087.

Chauris, H., Noble, M. S., Lambare, G., and Podvin, P., 2002a, Migration velocity analysis from locally coherent events in 2-D laterally heterogeneous media, Part I: Theoretical aspects: Geophysics, **67**, no. 04, 1202–1212.

——— 2002b, Migration velocity analysis from locally coherent events in 2-D laterally heterogeneous media, Part Ii: Applications on synthetic and real data: Geophysics, **67**, no. 04, 1213–1224.

Chavent, G., and Jacewitz, C. A., 1995, Determination of background velocities by multiple migration fitting: Geophysics, **60**, no. 02, 476–490.

Claerbout, J. F., 1985, Imaging the Earth's interior: , Blackwell Scientific Publications.

Clapp, R. G., Biondi, B., and Claerbout, J. F., 2004, Incorporating geologic information into reflection tomography: Geophysics, **69**, no. 2, 533–546.

Clayton, R. W., and Stolt, R. H., 1981, A born-WkBj inversion method for acoustic reflection data: Geophysics, **46**, no. 11, 1559–1567.

Clement, F., Chavent, G., and Gomez, S., 2001, Migration-based traveltime waveform inversion of 2-D simple structures: A synthetic example: Geophysics, **66**, no. 3, 845–860.

de Vries, D., and Berkhout, A. J., 1984, Velocity analysis based on minimum entropy: Geophysics, **49**, no. 12, 2132–2142.

Etgen, J., 1990, Residual prestack migration and interval-velocity estimation: , PhD thesis, Stanford University.

Faye, J. P., and Jeannot, J. P., 1986, Prestack migration velocities from focusing depth analysis: Prestack migration velocities from focusing depth analysis:, Soc. of Expl. Geophys., 56th Ann. Internat. Mtg., Session:S7.6.

Fletcher, R., Fowler, P., Kitchenside, P., and Albertin, U., 2006, Suppressing unwanted internal reflections in prestack reverse-time migration: Geophysics, **71**, E79–E82.

Fokkema, J., and Van Den Berg, P., 1993, Seismic applications of acoustic reciprocity: , Elsevier.

Fomel, S., Landa, E., and Turner, M., 2007, Poststack velocity analysis by separation and imaging of seismic diffractions: Geophysics, **72**, no. 6, U89–U94.

Fowler, P., 1988, Seismic velocity estimation using prestack time migration: , PhD thesis, Stanford University.

Gauthier, O., Virieux, J., and Tarantola, A., 1986, Two-dimensional nonlinear inversion of seismic waveforms - Numerical results: Geophysics, **51**, no. 07, 1387–1403.

Gray, S. H., Etgen, J., Dellinger, J., and Whitmore, D., 2001, Seismic migration problems and solutions: Geophysics, **66**, no. 5, 1622–1640.

Guitton, A., Kaelin, B., and Biondi, B., 2006, Least-square attenuation of reverse time migration artifacts: 75th Annual International Meeting, SEG, Expanded Abstracts, 2348–2352.

Halliday, D., Curtis, A., Vermeer, P., Strobbia, C., and Cluschenko, A., 2009, Source-receiver seismic interferometry: 78th Annual International Meeting, SEG, Expanded Abstracts, 4207–4210.

Harlan, W. S., Claerbout, J. F., and Rocca, F., 1984, Signal/noise separation and velocity estimation: Geophysics, **49**, no. 11, 1869–1880.

Lambare, G., Alerini, M., Baina, R., and Podvin, P., 2004, Stereotomography: a semi-automatic approach for velocity macromodel estimation: Geophys. Prosp., **52**, no. 6, 671–681.

Loewenthal, D., Lu, L., Robertson, R., and Sherwood, J., 1976, The Wave Equation applied to migration: Geophysical Prospecting, **24**, 380–399.

MacKay, S., and Abma, R., 1992, Imaging and velocity estimation with depth-focusing analysis: Geophysics, **57**, no. 12, 1608–1622.

MacKay, S., and Abma, R., 1993, Depth-focusing analysis using a wavefront-curvature criterion: Geophysics, **58**, no. 08, 1148–1156.

Mora, P., 1989, Inversion = migration + tomography: Geophysics, **54**, no. 12, 1575–1586.

Nemeth, T., 1995, Velocity estimation using tomographic depth-focusing analysis: Velocity estimation using tomographic depth-focusing analysis:, Soc. of Expl. Geophys., 65th Ann. Internat. Mtg, 465–468.

Nemeth, T., 1996, Relating depth-focusing analysis to migration velocity analysis: Relating depth-focusing analysis to migration velocity analysis:, Soc. of Expl. Geophys., 66th Ann. Internat. Mtg, 463–466.

Paffenholz, J., Stefani, J., McLain, B., and Bishop, K., 2002, SIgSbEe_2A Synthetic Subsalt Dataset - Image Quality as Function of Migration Algorithm and Velocity Model Error: SIgSbEe_2A Synthetic Subsalt Dataset - Image Quality as Function of Migration Algorithm and Velocity Model Error:, Eur. Assn. Geosci. Eng., 64th Mtg., B019.

Pratt, R. G., 1999, Seismic waveform inversion in the frequency domain, Part 1: Theory and verification in a physical scale model: Geophysics, **64**, no. 3, 888–901.

Rickett, J., and Sava, P., 2002, Offset and angle-domain common image-point gathers for shot-profile migration: Geophysics, **67**, no. 3, 883–889.

Romero, L. A., Ghiglia, D. C., Ober, C. C., and Morton, S. A., 2000, Phase encoding of shot records in prestack migration: Geophysics, **65**, no. 02, 426–436.

Sava, P., and Biondi, B., 2004a, Wave-equation migration velocity analysis - I: Theory: Geophysical Prospecting, **52**, 593–606.

——— 2004b, Wave-equation migration velocity analysis - II: Subsalt imaging examples: Geophysical Prospecting, **52**, 607–623.

Sava, P., and Fomel, S., 2003, Angle-domain common image gathers by wavefield continuation methods: Geophysics, **68**, no. 3, 1065–1074.

Sava, P., and Fomel, S., 2005, Coordinate-independent angle-gathers for wave equation migration: 75th Annual International Meeting, SEG, Expanded Abstracts, 2052–2055.

Sava, P., and Fomel, S., 2006, Time-shift imaging condition in seismic migration: Geophysics, **71**, no. 6, S209–S217.

Sava, P., Biondi, B., and Etgen, J., 2005, Wave-equation migration velocity analysis by focusing diffractions and reflections: Geophysics, **70**, U19–U27.

Shen, P., Symes, W., and Stolk, C. C., 2003, Differential semblance velocity analysis by wave-equation migration: Differential semblance velocity analysis by wave-equation migration:, Soc. of Expl. Geophys., 73rd Ann. Internat. Mtg., 2132–2135.

Sirgue, L., and Pratt, R., 2004, Efficient waveform inversion and imaging: A strategy for selecting temporal frequencies: Geophysics, **69**, no. 1, 231–248.

Stolt, R. H., and Weglein, A. B., 1985, Migration and inversion of seismic data: Geophysics, **50**, no. 12, 2458–2472.

Stork, C., 1992, Reflection tomography in the postmigrated domain: Geophysics, **57**, no. 05, 680–692.

Symes, W., 2009, Migration velocity analysis and waveform inversion: Geophysical Prospecting, **56**, 765–790.

Tarantola, A., 1987, Inverse Problem Theory: methods for data fitting and model parameter estimation: , Elsevier.

Vasconcelos, I., Snieder, R., and Douma, H., 2009a, Representation theorems and green's function retrieval for scattering in acoustic media: Phys. Rev. E, **80**, 036605.

——— 2009b, Wave-equation extended images via image-domain interferometry: 79th Annual International Meeting, SEG, Expanded abstracts.

Vasconcelos, I., 2008, Generalized representations of perturbed fields - applications in seismic interferometry and migration: 77th Annual International Meeting, SEG, Expanded Abstracts, 2927–2931.

Wapenaar, K., and Fokkema, J., 2006, Greens function representations for seismic interferometry: Geophysics, **71**, SI133–SI146.

Weglein, A. B., and Stolt, R. H., 1999, Migration-inversion revisited (1999): The Leading Edge, **18**, no. 8, 950–952.

Whitmore, N. D., 1995, An imaging hierarchy for common angle plane wave seismograms: , PhD thesis, University of Tulsa.

Woodward, M. J., 1992, Wave-equation tomography: Geophysics, **57**, no. 01, 15–26.

Yang, T., and Sava, P., 2009a, Moveout analysis of wave-equation extended images: Geophysics, submitted for publication.

——— 2009b, Wave-equation migration velocity analysis using extended images: 79th Annual International Meeting, SEG, Expanded abstracts.